IOPscience iopscience.iop.org

Home Search Collections Journals About Contact us My IOPscience

Relativistic spin-polarized scattering theory for space-filling potentials

This article has been downloaded from IOPscience. Please scroll down to see the full text article.

1993 J. Phys.: Condens. Matter 5 8005

(http://iopscience.iop.org/0953-8984/5/43/014)

View the table of contents for this issue, or go to the journal homepage for more

Download details:
IP Address: 171.66.16.96
The article was downloaded on 11/05/2010 at 02:06

Please note that terms and conditions apply.

J. Phys.: Condens. Matter 5 (1993) 8005–8030. Printed in the UK

Relativistic spin-polarized scattering theory for space-filling potentials

S C Lovatt†, B L Gyorffy† and G Y Guo‡

† H H Wills Physics Laboratory, University of Bristol, Tyndall Avenue, Bristol, Avon, UK
‡ SERC Daresbury Laboratory, Warrington, Cheshire, UK

Received 9 July 1993

Abstract. Relativistic potential scattering from non-spherically symmetric scatterers is studied and expressions for both charge and magnetization density are derived. The validity of full-potential Korringer–Kohn–Rostoker (KKR) multiple-scattering theory for full potentials is asserted and a practical scheme for calculating the single-site t-matrix for the space-filling Wigner–Seitz cell is then described. Results, including full-potential band-structure calculations for silicon with an L_{max} of two, three and four, are then presented.

1. Introduction

Generally, the application of multiple-scattering theory [1] for describing electrons in condensed-matter systems involves representing each scattering site (i.e. atom or ion) as a potential well that is both isotropic and of finite range. This is called the muffin-tin approximation, after the sphere delimiting the potential well. More recent work has tended to relax this restriction [2–7], and the problem of treating unrestricted space-filling potentials has been addressed repeatedly [8–12]. In this paper we develop an efficient computational technique for studying relativistic potential scattering from non-spherically symmetric scatterers. Although our discussion will at first be quite general, we shall have in mind applications in the calculation of the electronic structure of solids, and in the latter part of the paper we illustrate our method using crystalline silicon and ferromagnetic iron as explicit examples.

There are a number of physical effects where potential anisotropy can be expected to play a significant role. These include the magneto-crystalline anisotropy of transition metals such as iron and nickel, covalent bonding, surface effects in metals and the unexplained degrees of freedom observed in heavy-fermion systems. In such cases, it is important to treat spin polarization together with orbit–orbit and spin–orbit coupling on equal footings. Experience suggests that perturbation methods cannot be trusted in these circumstances [13], and hence the exact scattering-theory methods described below can be expected to have a wide field of useful applications.

Following Strange *et al* [2], the applicability of relativistic density functional theory [14] is assumed, and the influence of the effective magnetic field on the orbital motion of the electrons (diamagnetism) is ignored. The former assumption allows all many-body effects to be packaged as effective exchange–correlation potentials. The latter restricts the magnetic vector potential so that it gives rise to a 'spin-only' effective B-field. This procedure is known as the Gordon decomposition [15, 16].

0953-8984/93/438005+26$07.50 © 1993 IOP Publishing Ltd

In section 2, starting from first principles, we formulate the single-site scattering problem and solve it directly for a spherically confined but anisotropic (warped muffin-tin) potential. In section 3 we review how the **t**-matrix can be obtained, and continue by discussing angular-momentum truncation in section 4. We generalize our technique, as required for a space-filling potential defined within a Wigner–Seitz cell, and discuss the angular-momentum convergence of our **t**-matrix calculation scheme in section 5. In section 6 we show how the charge and magnetization densities can be calculated in our approach. Finally, we present results for iron and silicon in section 7 and summarize our conclusions in section 8.

The following notation has been adopted in what follows. Dirac four-component spinors are given a *tilde*, e.g. $\tilde{\psi}$. Two-component spinors are given a *bar*, e.g. $\bar{\psi}$. Three-component real-space vectors are printed in bold italics, and unit vectors given a *hat*, e.g. $\boldsymbol{W}(\hat{\boldsymbol{r}})$. Matrices are underlined whenever their indices are suppressed e.g. $\underline{\mathbf{A}}$, $\underline{\beta}$.

2. The single-site scattering problem

Neglecting diamagnetism, the Kohn–Sham–Dirac equation of relativistic density functional theory reduces to [2]

$$\left\{-\mathrm{i}\hbar c\underline{\alpha}\cdot\boldsymbol{\nabla}+m_{\mathrm{e}}c^2\underline{\beta}+U_{\mathrm{eff}}[\boldsymbol{r};(n,\boldsymbol{m})]+\underline{\beta}\underline{\boldsymbol{\sigma}}\cdot\boldsymbol{W}_{\mathrm{eff}}[\boldsymbol{r};(n,\boldsymbol{m})]-\varepsilon\right\}\tilde{\psi}(\boldsymbol{r}) \;=\; 0 \qquad (1)$$

where $\underline{\alpha}$ and $\underline{\beta}$ are the standard *four by four* Dirac matrices [16], and $\tilde{\psi}(\boldsymbol{r})$ is a four-component Dirac spinor wavefunction.

In the case of application to solids, U_{eff} and $\boldsymbol{W}_{\mathrm{eff}}$ are periodic crystal potentials, composed of individual potential wells, namely $U_{\mathrm{eff}} = \sum_i U(\boldsymbol{r}-\boldsymbol{R}_i)$ and $\boldsymbol{W}_{\mathrm{eff}} = \sum_i \boldsymbol{W}(\boldsymbol{r}-\boldsymbol{R}_i)$.

As a preliminary to solving equation (1), we shall study the Dirac equation

$$\left\{c\underline{\alpha}\cdot\boldsymbol{p}+m_{\mathrm{e}}c^2\underline{\beta}+U(\boldsymbol{r})+\underline{\beta}\underline{\boldsymbol{\sigma}}\cdot\boldsymbol{W}(\boldsymbol{r})-\varepsilon\right\}\tilde{\psi}(\boldsymbol{r})=0 \qquad (2)$$

for a U and $\boldsymbol{W}$ describing a single scattering centre.

As is well known [16], $\underline{\alpha}\cdot\boldsymbol{p} = -\mathrm{i}\hat{\boldsymbol{r}}\cdot\underline{\alpha}[\hbar(\partial/\partial r)+(1/r)(\hbar-\underline{\beta}\underline{\kappa})]$, and equation (2) can be written in the following convenient form:

$$\left\{m_{\mathrm{e}}c^2\underline{\beta}\;+\;V(\boldsymbol{r})\;-\;\mathrm{i}\hbar c\cdot\underline{\alpha}\left[(1/r)\left(\hbar-\underline{\beta}\underline{\kappa}\right)+\hbar(\partial/\partial r)\right]\right\}\tilde{\psi}(\boldsymbol{r}) \;=\; \varepsilon\tilde{\psi}(\boldsymbol{r}) \qquad (3)$$

where $\underline{\kappa} = \underline{\beta}(\underline{\boldsymbol{\sigma}}\cdot\mathbf{L}+\hbar)$.

The principal virtue of this version of the Dirac equation is that it makes the introduction of the radial wavefunctions particularly straightforward. In short, we proceed by expanding $\tilde{\psi}(\boldsymbol{r})$ in spin-angular harmonics, by writing

$$\tilde{\psi}(\boldsymbol{r}) \;=\; \sum_{\kappa,\mu}\begin{bmatrix}\bar{\chi}_{\kappa,\mu}(\hat{\boldsymbol{r}}) & f_{\kappa,\mu}(r)\\ \bar{\chi}_{-\kappa,\mu}(\hat{\boldsymbol{r}}) & g_{\kappa,\mu}(r)\end{bmatrix} \text{ where } \bar{\chi}_{\kappa,\mu}(\hat{\boldsymbol{r}}) \;=\; \begin{bmatrix}C^{\kappa,\mu}_{l,(\mu-1/2);1/2,+1/2} & Y_\ell^{\mu-1/2}(\hat{\boldsymbol{r}})\\ C^{\kappa,\mu}_{l,(\mu+1/2);1/2,-1/2} & Y_\ell^{\mu+1/2}(\hat{\boldsymbol{r}})\end{bmatrix}$$

is a Pauli column spinor eigenfunction of the total angular-momentum operator, $J^2 = |\boldsymbol{L}+\boldsymbol{S}|^2$, and also its z component, $J_Z = L_Z + S_Z$.

If $V(\boldsymbol{r})$ is isotropic, equation (3) only relates the *large component*, $f_{\kappa,\mu}(r)$, to itself (via $m_{\mathrm{e}}c^2\underline{\beta}+V(\boldsymbol{r})$) and to the *small component* $g_{\kappa,\mu}(r)$ (via the term in $\hat{\boldsymbol{r}}\cdot\underline{\alpha}$), and so the Dirac equation can be separated into an infinite set of pairs of first-order differential equations. If $V(\boldsymbol{r})$ is not isotropic, it introduces couplings between the angular-momentum channels as follows:

$$\sum_{\kappa',\mu'}\left\{\left[\mathrm{i}\hbar c\underline{\sigma}_y\left(\frac{\mathrm{d}}{\mathrm{d}r}+\frac{1}{r}+\frac{\kappa}{r}\underline{\sigma}_z\right)-m_{\mathrm{e}}c^2\underline{\sigma}_z+\varepsilon\right]\delta_{\kappa',\kappa}\delta_{\mu',\mu}-V_{\kappa,\mu;\kappa',\mu'}(\boldsymbol{r})\right\}\bar{\mathsf{R}}_{\kappa',\mu'}(r)=0 \qquad (4)$$

where $\tilde{R}_{\kappa,\mu} = \begin{Bmatrix} f_{\kappa',\mu'}(r) \\ g_{\kappa',\mu'}(r) \end{Bmatrix}$ is a two component radial wavefunction, and

$$V_{\kappa,\mu;\kappa',\mu'}(\boldsymbol{r}) = \int_{4\pi} \begin{bmatrix} \bar{\chi}^{\dagger}_{\kappa,\mu}(\hat{\boldsymbol{r}}) U(\boldsymbol{r}) \bar{\chi}_{\kappa',\mu}(\hat{\boldsymbol{r}}) & 0 \\ 0 & \bar{\chi}^{\dagger}_{-\kappa,\mu}(\hat{\boldsymbol{r}}) U(\boldsymbol{r}) \bar{\chi}_{-\kappa',\mu}(\hat{\boldsymbol{r}}) \end{bmatrix} \mathrm{d}^2\hat{\boldsymbol{r}}$$
$$+ \int_{4\pi} \begin{bmatrix} \bar{\chi}^{\dagger}_{\kappa,\mu}(\hat{\boldsymbol{r}}) \boldsymbol{W}(\boldsymbol{r}) \cdot \boldsymbol{\sigma} \bar{\chi}_{\kappa',\mu}(\hat{\boldsymbol{r}}) & 0 \\ 0 & \bar{\chi}^{\dagger}_{-\kappa,\mu}(\hat{\boldsymbol{r}}) \boldsymbol{W}(\boldsymbol{r}) \cdot \boldsymbol{\sigma} \bar{\chi}_{-\kappa',\mu}(\hat{\boldsymbol{r}}) \end{bmatrix} \mathrm{d}^2\hat{\boldsymbol{r}}.$$

If $U(\boldsymbol{r})$ and $\boldsymbol{W}(\boldsymbol{r})$ are spherically symmetric and $\boldsymbol{W}(\boldsymbol{r})$ is unidirectional, the V-matrix simplifies so that only those pairs of channels with identical μ and l values ($\kappa = -(\kappa' + 1)$ or $\kappa = \kappa'$) are coupled. However, if either U or $\boldsymbol{W}$ is anisotropic, V becomes more complicated.

To be more specific about V, we expand U and $\boldsymbol{W}$ in spherical harmonics:

$$\begin{aligned} U(\boldsymbol{r}) &= \sum_{LM} U^{LM}(r)\, Y_L^M(\hat{\boldsymbol{r}}) \\ \boldsymbol{W}(\boldsymbol{r}) &= \sum_{LM} \boldsymbol{W}^{LM}(r)\, Y_L^M(\hat{\boldsymbol{r}}) \end{aligned} \tag{5}$$

and find that

$$V_{\kappa_1,\mu_1;\kappa_2,\mu_2}(r) = \sum_{LM} U^{LM}(r) \begin{bmatrix} \langle \kappa_1, \mu_1 | Y_L^M | \kappa_2, \mu_2 \rangle & 0 \\ 0 & \langle -\kappa_1, \mu_1 | Y_L^M | -\kappa_2, \mu_2 \rangle \end{bmatrix}$$
$$+ \sum_{LM} \boldsymbol{W}^{LM}(r) \cdot \begin{bmatrix} \langle \kappa_1, \mu_1 | \boldsymbol{\sigma} Y_L^M | \kappa_2, \mu_2 \rangle & 0 \\ 0 & \langle -\kappa_1, \mu_1 | \boldsymbol{\sigma} Y_L^M | -\kappa_2, \mu_2 \rangle \end{bmatrix} \tag{6}$$

where

$$\langle \kappa_1, \mu_1 | Y_L^M | \kappa_2, \mu_2 \rangle$$
$$= C^{\kappa_1,\mu_1}_{\ell_1,\mu_1-1/2;1/2,+1/2} C^{\kappa_2,\mu_2}_{\ell_2,\mu_2-1/2;1/2,+1/2} \int_{4\pi} \left[Y_{\ell_1}^{\mu_1-1/2}(\hat{\boldsymbol{r}}) \right]^* Y_L^M(\hat{\boldsymbol{r}}) Y_{\ell_2}^{\mu_2-1/2}(\hat{\boldsymbol{r}})\, \mathrm{d}^2\hat{\boldsymbol{r}}$$
$$+ C^{\kappa_1,\mu_1}_{l_1,\mu_1+1/2;1/2,-1/2} C^{\kappa_2,\mu_2}_{l_2,\mu_2+1/2;1/2,-1/2} \int_{4\pi} \left[Y_{\ell_1}^{\mu_1+1/2}(\hat{\boldsymbol{r}}) \right]^* Y_L^M(\hat{\boldsymbol{r}}) Y_{\ell_2}^{\mu_2+1/2}(\hat{\boldsymbol{r}})\, \mathrm{d}^2\hat{\boldsymbol{r}}$$

are Gaunt Numbers for half-integral angular momenta.

The corresponding terms in the second sum of equation (6) are spin-orientation vectors, and are dotted into the $\boldsymbol{W}^{LM}$, as indicated. Their x and y components can be obtained in terms of Gaunt numbers after expressing σ_x and σ_y in terms of spin-raising and -lowering operators:

$$\langle \kappa_1, \mu_1 | Y_L^M\, \sigma_x | \kappa_2, \mu_2 \rangle = \tfrac{1}{2} \langle \kappa_1, \mu_1 | Y_L^M | \kappa_2, \mu_2 + 1 \rangle \left[j_2(j_2+1) - \mu_2(\mu_2 - 1) \right]^{1/2}$$
$$+ \tfrac{1}{2} \langle \kappa_1, \mu_1 | Y_L^M | \kappa_2, \mu_2 - 1 \rangle \left[j_2(j_2+1) - \mu_2(\mu_2 + 1) \right]^{1/2}$$
$$\langle \kappa_1, \mu_1 | Y_L^M\, \sigma_y | \kappa_2, \mu_2 \rangle = (\mathrm{i}/2) \langle \kappa_1, \mu_1 | L_L^M | \kappa_2, \mu_2 + 1 \rangle \left[j_2(j_2+1) - \mu_2(\mu_2 - 1) \right]^{1/2}$$
$$- (\mathrm{i}/2) \langle \kappa_1, \mu_1 | Y_L^M | \kappa_2, \mu_2 - 1 \rangle \left[j_2(j_2+1) - \mu_2(\mu_2 + 1) \right]^{1/2}.$$

The z components can be obtained more directly:

$$\begin{aligned}\langle \kappa_1, \mu_1 | Y_L^M \ \sigma_z | \kappa_2, \mu_2 \rangle = {} & C^{\kappa_1,\mu_1}_{\ell_1,\mu_1-1/2;1/2,+1/2} C^{\kappa_2,\mu_2}_{\ell_2,\mu_2-1/2;1/2,+1/2} \\ & \times \int_{4\pi} \left[Y^{\mu_1-1/2}_{\ell_1}(\hat{r}) \right]^* Y^M_L(\hat{r}) Y^{\mu_2-1/2}_{\ell_2}(\hat{r}) \, \mathrm{d}^2\hat{r} \\ & - C^{\kappa_1,\mu_1}_{\ell_1,\mu_1+1/2;1/2,-1/2} C^{\kappa_2,\mu_2}_{\ell_2,\mu_2+1/2;1/2,-1/2} \\ & \times \int_{4\pi} \left[Y^{\mu_1+1/2}_{\ell_1}(\hat{r}) \right]^* Y^M_L(\hat{r}) Y^{\mu_2+1/2}_{\ell_2}(\hat{r}) \, \mathrm{d}^2\hat{r}.\end{aligned}$$

The symmetry properties of these kinematic matrix elements are such that V is Hermitian, even when U and W are not isotropic.

For practical calculations, the infinite set of coupled equations is simplified by approximating them with a sub-set defined by an (arbitrary) maximum angular momentum, $L_{\max}$. The truncated coupling matrix (and hence the Hamiltonian) remains Hermitian, because the cut-off is symmetric in eigenstate labels. That $V_{\kappa_1,\mu_1;\kappa_2,\mu_2}$ may be truncated in this way is justified in section 4 below.

3. Finding the 'on-the-energy-shell' t-matrix

For many purposes, the scattering problem is solved once the 'on-the-energy-shell' **t**-matrix has been obtained. This can be done as follows [17]. First, a basis $\{\tilde{\Phi}_Q\}$ is sought that spans all solutions of the scattering Hamiltonian that are regular at the origin. This basis need not be orthonormal. The angular-momentum representation of the **s**-matrix can then be obtained by identifying every linear combination of these $\{\tilde{\Phi}_Q\}$ for which incoming flux is present in one spin-angular symmetry channel *only*.

If near to the origin the scattering potential depends only on $|r|$, a suitable set of regular functions can be defined by stipulating that each has a particular and unique spin-angular symmetry at the *origin*, $Q \to (\kappa, \mu)$. Each basis function $\tilde{\Phi}_Q(r)$ can then be constructed by outwards integration of (4) from the boundary condition asserted for it at the origin [18, 2]. As usual, the $r \to \infty$ asymptotic form of these functions can be expressed in terms of four-component spinor Hankel functions, $\tilde{h}^{\pm}_{\Lambda}$, where Λ from now on always stands for *asymptotic* angular-momentum labels (κ, μ).

Technically, we define

$$\tilde{h}^{\pm}_{\kappa,\mu}(r;\varepsilon) = \left(\frac{q}{4\pi\hbar^2 c^2} \right)^{1/2} \begin{bmatrix} \left(\varepsilon + m_e c^2\right)^{1/2} & \tilde{\chi}_{\kappa,\mu}(\hat{r}) & h^{\pm}_{\ell}(qr) \\ \mathrm{i}S_\kappa \left(\varepsilon - m_e c^2\right)^{1/2} & \tilde{\chi}_{-\kappa,\mu}(\hat{r}) & h^{\pm}_{\tilde{\ell}}(qr) \end{bmatrix} \tag{7}$$

where the energy ε and radial momentum $\hbar q$ are, of course, related by

$$(hcq)^2 = \varepsilon^2 - \left(m_e c^2\right)^2$$

and we have adopted Dirac normalization such that

$$\begin{aligned}\int_{\infty} \left[\tilde{f}^{\pm}_{\Lambda}(r;\varepsilon) \right]^{\dagger} \tilde{f}^{\pm}_{\Lambda}(r;\varepsilon') \, \mathrm{d}^3 r &= \frac{\varepsilon}{\hbar^2 c^2 q} \frac{1}{2\pi} \int_{-\infty}^{\infty} \exp[\pm r(q - q')] \, \mathrm{d}r \\ &= \frac{\mathrm{d}q}{\mathrm{d}\varepsilon} \delta(q - q') \ = \ \delta(\varepsilon - \varepsilon')\end{aligned}$$

where $\tilde{f}_{\Lambda} = 1/2(\tilde{h}^{+}_{\Lambda} + \tilde{h}^{-}_{\Lambda})$.

We now seek $\tilde{\Phi}_Q(r;\varepsilon)$ in the form

$$\lim_{r\to 0}\tilde{\Phi}_{\kappa,\mu}(r;\varepsilon)=\begin{bmatrix}\bar{\chi}_{\kappa,\mu}(\hat{r}) & f_\kappa(r;\varepsilon,Z)\\ \bar{\chi}_{-\kappa,\mu}(\hat{r}) & \mathrm{i}g_\kappa(r;\varepsilon,Z)\end{bmatrix}$$

where f_κ and g_κ are radial functions specified close to the origin in terms of the series solution of the hydrogenic Dirac Hamiltonian [19]. This is preferred to the value given in [18], as it avoids the requirement associated with that value and positive κ for a radial grid extending in excessively close to the origin.

In the opposite ($r\to\infty$) limit, $\tilde{\Phi}_Q$ contains radial components in many other angular-momentum channels. In fact it can be written as

$$\lim_{r\to\infty}\tilde{\Phi}_Q(r)=\sum_\Lambda \tilde{h}^+_\Lambda(r)\,\mathbf{a}_{\Lambda,Q}+\tilde{h}^-_\Lambda(r)\,\mathbf{b}_{\Lambda,Q}. \tag{8}$$

Multiplying $\tilde{\Phi}_{Q'}$ on the right by $\mathbf{b}^{-1}_{Q',\Lambda}$, and summing over Λ', we define a new function, $\tilde{\chi}_\Lambda$

$$\tilde{\chi}_\Lambda(r)=\sum_Q \tilde{\Phi}_Q(r)\mathbf{b}^{-1}_{Q,\Lambda}. \tag{9}$$

It follows from (8) and (9) that, asymptotically, $\tilde{\chi}_\Lambda$ consists of a single incoming spherical wave and a sum of outgoing waves

$$\lim_{r\to\infty}\{\tilde{\chi}_\Lambda(r)\} \;=\; \tilde{h}^-_\Lambda(r)+\sum_{\Lambda'}\tilde{h}^+_{\Lambda'}(r)\sum_Q \mathbf{a}_{\Lambda',Q}\,\mathbf{b}^{-1}_{Q,\Lambda}.$$

The $\{\tilde{\chi}_\Lambda\}$ are the spherical-wave analogues of the familiar plane-wave scattering solutions, and form a complete set. Consequently, the angular-momentum representation of the **s**-matrix, which is defined by the asymptotic relation

$$\tilde{\chi}_\Lambda(r)=\tilde{h}^-_\Lambda(r)+\sum_{\Lambda'}\tilde{h}^+_{\Lambda'}(r)\mathbf{s}_{\Lambda',\Lambda}$$

is given by

$$\mathbf{s}=\mathbf{a}\mathbf{b}^{-1}. \tag{10}$$

Furthermore, the 'on-the-energy-shell' components of the **t**-matrix we require [20] are defined by the relation

$$-2\mathrm{i}q\,\mathbf{t}_{\kappa_1,\mu_1,\kappa_2,\mu_2}=\mathbf{s}_{\kappa_1,\mu_1,\kappa_2,\mu_2}-\delta_{\kappa_1,\kappa_2}\delta_{\mu_1,\mu_2}. \tag{11}$$

We now turn to the calculation of the **a** and **b** matrices. Evidently, they are the expansion coefficients of the $\tilde{\Phi}_Q$ in the κ,μ basis beyond the range of the potential, and are defined by equation (8). They can be written as integrals of the Wronskians of the value of $\tilde{\Phi}$ and free-space solutions $\tilde{h}^\pm_\Lambda$ taken over any surface Γ enclosing the region where $V(r)$ is non-zero, namely

$$\begin{aligned}\mathbf{a}_{\Lambda,Q}&=-W_\Gamma\left[\tilde{h}^+_\Lambda;\tilde{\Phi}_Q\right]/W_0\\ \mathbf{b}_{\Lambda,Q}&=+W_\Gamma\left[\tilde{h}^-_\Lambda;\tilde{\Phi}_Q\right]/W_0\end{aligned} \tag{12}$$

where the relativistic Wronskians $W_\Gamma[\bar{h}_\Lambda^\pm; \tilde{\psi}]$ and W_0 are defined by the following relations

$$W_\Gamma\left[\bar{h}_\Lambda^\pm(r); \tilde{\psi}(r)\right] = \mathrm{i}\int_\Gamma \left[\bar{h}_\Lambda^\mp(r)\right]^\dagger \, \alpha \, \tilde{\psi}(r) \cdot \mathrm{d}^2 r$$

$$W_0(r;\varepsilon) = \mathrm{i}r^2 \int_{4\pi} \left[\bar{h}_\Lambda^-(r)\right]^\dagger \, \alpha \, \bar{h}_\Lambda^-(r) \, \mathrm{d}^2\hat{r} \;\; = \;\; -\frac{\mathrm{i}}{2\pi\hbar c}. \tag{13}$$

In the warped muffin-tin case, the natural surface over which to conduct the Wronskian integral is the muffin-tin sphere itself. This has two distinct advantages. First, there is then no need to continue the radial integrals across the potential step that generally occurs at the muffin-tin radius; and second, the surface integrals become trivial because of the orthonormality of the spin-angular harmonics on such surfaces.

$$\mathrm{i}r^2 \int_{4\pi} \bar{h}_\Lambda^{\pm\dagger}(r) \, \alpha \, \bar{\Phi}_Q(r) \cdot \mathrm{d}^2\hat{r} = \bar{h}_{\Lambda;1}^\mp(r) \, \bar{\Phi}_{Q;2}(r) - \bar{h}_{\Lambda;2}^\mp(r) \, \bar{\Phi}_{Q;1}(r)$$

where

$$\bar{\Phi}_Q(r) = \sum_{\kappa,\mu} \begin{bmatrix} \tilde{\chi}_{\kappa,\mu}(\hat{r}) & \bar{\Phi}_{\kappa,\mu,Q;1}(r) \\ \tilde{\chi}_{-\kappa,\mu}(\hat{r}) & \mathrm{i}\bar{\Phi}_{\kappa,\mu,Q;2}(r) \end{bmatrix}.$$

In short, we find that

$$\begin{aligned} \mathbf{a}_{\Lambda,Q}(R,\varepsilon) = +\mathrm{i}R\left[\pi q\left(\varepsilon + m_\mathrm{e}c^2\right)\right]^{\frac{1}{2}}/2\Big\{ & h_\ell^-(qR)\bar{\Phi}_{\Lambda,Q;2}(R;\varepsilon) \\ & - \left[\hbar c q S_\kappa/(\varepsilon + m_\mathrm{e}c^2)\right] h_{\tilde{\ell}}^-(qR)\bar{\Phi}_{\Lambda,Q;1}(R;\varepsilon)\Big\} \\ \mathbf{b}_{\Lambda,Q}(R,\varepsilon) = -\mathrm{i}R\left[\pi q\left(\varepsilon + m_\mathrm{e}c^2\right)\right]^{\frac{1}{2}}/2\Big\{ & h_\ell^+(qR)\bar{\Phi}_{\Lambda,Q;2}(R;\varepsilon) \\ & - \left[\hbar c q S_\kappa/(\varepsilon + m_\mathrm{e}c^2)\right] h_{\tilde{\ell}}^+(qR)\bar{\Phi}_{\Lambda,Q;1}(R;\varepsilon)\Big\}. \end{aligned} \tag{14}$$

The eigenvectors (and associated eigenphases) of the **s**-matrix can be labelled by their limiting spin-angular character at zero energy

$$\mathbf{s}(\varepsilon)\, u_\nu(\varepsilon) = \exp\left[2\mathrm{i}\delta_\nu(\varepsilon)\right] u_\nu(\varepsilon)$$

$$u_\nu^\dagger(\varepsilon) = \left(u_{\nu;\kappa_1,\mu_1}^*(\varepsilon)\,,\; u_{\nu;\kappa_2,\mu_2}^*(\varepsilon),\; \cdots, u_{\nu;\kappa_l,\mu_l}^*(\varepsilon),\; \cdots\right)$$

where the asymptotic form of the corresponding eigenfunction of the Hamiltonian is

$$\Psi_\nu(\varepsilon) = \sum_{\kappa,\mu} \mu_{\nu;\kappa,\mu}(\varepsilon) \begin{bmatrix} \tilde{\chi}_{\kappa,\mu}(\hat{r})\; j_\ell(qr + \delta_\nu) \\ \mathrm{i}\tilde{\chi}_{-\kappa,\mu}(\hat{r})\; j_{\tilde{\ell}}(qr + \delta_\nu) \end{bmatrix}.$$

In the $\varepsilon \to 0$ limit, the eigenvector $u_\nu(0)$ has only one non-zero component, namely

$$\lim_{\varepsilon\to 0} u_{\nu;\kappa_n,\mu_i}(\varepsilon) = \delta_{n,\nu}. \tag{15}$$

Hence it is possible to identify ν with (κ, μ) and to speak of (for example) an S-like phase shift, meaning minus half of that eigenphase of the **s**-matrix associated with the eigenvector of the **s**-matrix that evolved from the zero-kinetic-energy eigenvector that represented a pure S wave.

4. Angular-momentum truncation

It is inevitable that above some angular-momentum L_{max} the **s**-matrix reduces to the identity. It is less obvious that the coupled equations and the **a** and **b** matrices can be similarly truncated. We now turn to these related questions.

As regards the coupled equations, there is a marked tendency for low angular-momentum radial components to induce very large responses in those high angular-momentum channels to which they are coupled. This 'enhanced *up scattering*' can be understood mathematically in terms of the power-law behaviour of spherical Bessel functions close to the origin, and also physically as representing the formation of those sharply defined incident wave-fronts that pierce the anisotropic potential on precisely those trajectories that avoid picking up much angular-momentum from the potential.

The above observations might be taken to suggest that truncation of the **t**-matrix at L_{max} is misguided, as it involves ignoring high angular-momentum components of considerable magnitude. Fortunately, the secondary effect on the low-angular-momentum channels of the large amplitudes in the high angular-momentum channels is negligible, because *down scattering* is suppressed to a much greater degree than *up scattering* is enhanced. Hence, if it can be shown that only the radial functions in the low angular-momentum channels play a significant part in determining the **s**-matrix, then L_{max} truncation has been justified.

To be more specific, numerical experience (once more consistent with the power-law behaviour of the j_l and n_l functions close to the origin), implies that **a** and **b** have the following approximate structures

$$\mathbf{a} = \begin{bmatrix} \mathbf{A} & \mathbf{0} \\ \mathbf{J} & \mathbf{K} \end{bmatrix} \qquad \mathbf{b} = \begin{bmatrix} \mathbf{B} & \mathbf{0} \\ \mathbf{J} & \mathbf{K} \end{bmatrix}$$

and hence

$$\mathbf{b}^{-1} = \begin{bmatrix} \mathbf{B}^{-1} & \mathbf{0} \\ -\mathbf{K}^{-1}\mathbf{J}\,\mathbf{B}^{-1} & \mathbf{K}^{-1} \end{bmatrix}.$$

Consequently,

$$\mathbf{s} = \begin{bmatrix} \mathbf{A}\,\mathbf{B}^{-1} & \mathbf{0} \\ \mathbf{0} & \mathbf{1} \end{bmatrix}.$$

Evidently, if the **a** and **b** matrices had exactly the form shown, the low angular-momentum sector of **s** would be given exactly by $\mathbf{A}\,\mathbf{B}^{-1}$. In reality, the upper right-hand sub matrices (shown above as identically zero) contain small non-zero entries, Ω_a and Ω_b, and the **J** and **K** which are shown as common to the **a** and **b** matrices differ slightly between them. To first order in all deviations from the ideal forms of **a** and **b**, the low angular-momentum sector $\mathbf{s}_{L_{max}}$ of the **s**-matrix, is given by

$$\mathbf{s}_{L_{max}} = \mathbf{A}\mathbf{B}^{-1} + \left[\mathbf{A}\mathbf{B}^{-1}\Omega_b - \Omega_a\right]\mathbf{K}^{-1}\mathbf{J}\mathbf{B}^{-1}.$$

$\mathbf{J}_a - \mathbf{J}_b$ and $\mathbf{K}_a - \mathbf{K}_b$ only enter into the expansion of $\mathbf{s}_{L_{max}}$ via second-order and higher terms. It is apparent that the error introduced into $\mathbf{s}_{L_{max}}$ by truncating the **a** and **b** matrices to **A** and **B** (and so discarding all terms after $\mathbf{A}\mathbf{B}^{-1}$) is small, being first order in the Ω matrices. This establishes the legitimacy of L_{max} truncation both of the potential expansion in equation (5) and of the **a** and **b** matrices.

5. Space-filling potentials

The question of the applicability of multiple-scattering theory to space-filling potentials is contested in the literature. In particular, whether 'near-field corrections' have to be made has been much discussed [21, 22, 8].

We agree with Butler *et al* [11] that the formalism of multiple-scattering theory holds for space-filling potentials as long as the **s**-matrices involved are evaluated on the surface of the Wigner–Seitz cells. Moreover, we accept Nesbet's argument [9] that for the full-potential problem, the local cell potential can be arbitrarily continued into the *moon regions* [8] between the surface of the Wigner–Seitz cell, Γ_{WS}, and its circumsphere in order to simplify the calculation of its **s**-matrix, and that the basis functions so generated are independent of the potential in the moon regions.

Once the **t**-matrix $\mathbf{t}_{\Lambda',\Lambda}(\varepsilon)$ has been calculated, we proceed to finding the energy bands by looking for the zeroes of the generalized KKR determinant. Namely, for each wave vector k, we find the energies $\varepsilon_{k,\gamma}$, such that

$$||\mathbf{t}^{-1}(\varepsilon) - \mathrm{i}q - \mathbf{B}(k;\varepsilon)|| \;=\; 0$$

where $B_{\Lambda',\Lambda}(k;\varepsilon)$ are the relativistic structure constants [23, 20, 2].

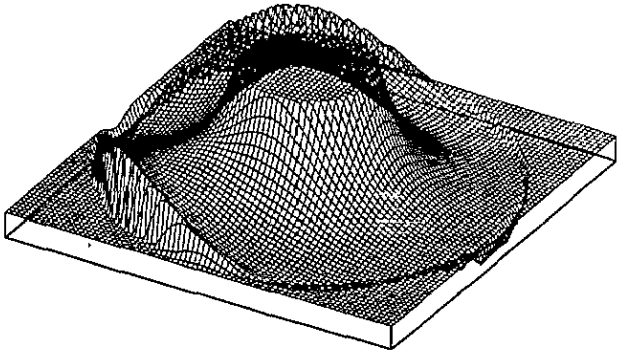

Figure 1. Analyticaly continued silicon potential extending throughout the Wigner–Seitz circumsphere.

The two obvious candidates for 'moon-region' potential are (i) that which continues the interior scattering potential smoothly, so that the simplest possible representation of the Hamiltonian within the Wigner–Seitz circumsphere can be used [12], see figure 1 or (ii) *zero* [24], so that **s** can be evaluated on the Wigner–Seitz circumsphere, see figure 2. We next argue that there is no advantage to be gained from requiring the potential within the Wigner–Seitz circumsphere to be smooth. By contrast, the practical advantage of evaluating **s** on the Wigner–Seitz circumsphere, which can only be done if the potential in the moon regions is set to zero, is obvious.

Because the choice of Wigner–Seitz cell potential we favour is discontinuous on Γ_{WS}, it cannot be accurately represented without the use of high-order spherical harmonics.

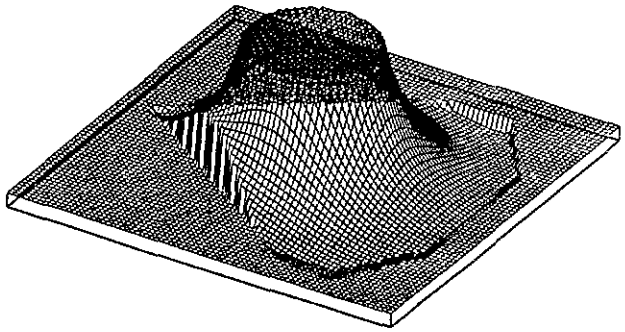

Figure 2. Abruptly truncated silicon potential, limited to within the Wigner–Seitz cell.

Fortunately, such high-order harmonics do not enter into the truncated set of radial equations. The couplings they give rise to all involve high angular-momentum channels (because of the *triangle rule*). So far as it is legitimate to neglect such high angular-momentum channels, to that *same* extent the high-order components of the potential can be neglected. Moreover, the $L_{\max}$ defining the set of radial equations fixes the point at which the potential expansion can be truncated, namely $\frac{1}{2}L_{\max}$. It follows that a space-filling potential can be adequately expressed *throughout each Wigner–Seitz cell* in terms of a very limited number of spherical harmonics. In all our calculations, we have found **s** (and so **t**) by integrating (4), and evaluating the **a** and **b** matrices using (14), at the radius of the Wigner–Seitz circumsphere.

6. Charge and magnetization densities

While the 'on-the-energy-shell' **t**-matrix for every unit cell is sufficient to determine the energy eigenvalues of an infinite solid, in a self-consistent calculation the charge and magnetization densities are required as well. In this section we discuss the formulae for these quantities appropriate to the anisotropic scatterers considered here. Recall that the charge and magnetization densities may be calculated using the following formal relations:

$$\begin{aligned} q(\boldsymbol{r};\varepsilon) &= e\,\langle \boldsymbol{r}|\,\delta(\varepsilon - H)\,|\boldsymbol{r}\rangle \\ \boldsymbol{m}(\boldsymbol{r};\varepsilon) &= \mu_{\text{Bohr}}\,\langle \boldsymbol{r}|\,\boldsymbol{\beta\sigma}\,\delta(\varepsilon - H)\,|\boldsymbol{r}\rangle\,. \end{aligned} \tag{16}$$

Resolving the identity to the right of the delta function in the first of equation (16) using the spherical scattering solutions [25] gives:

$$q(\boldsymbol{r};\varepsilon) = e\sum_{E,\Lambda}\tilde{\chi}^{\dagger}_{\Lambda}(\boldsymbol{r};E)\delta(\varepsilon - E)\tilde{\chi}_{\Lambda}(\boldsymbol{r};E) = e\sum_{\Lambda}\int^{\infty}\tilde{\chi}^{\dagger}_{\Lambda}(\boldsymbol{r};E)\delta(\varepsilon - E)\tilde{\chi}_{\Lambda}(\boldsymbol{r};E)\,\mathrm{d}E. \tag{17}$$

We now recast the above relation into a form more suitable for numerical calculations. Changing the variable of integration, and using the relativistic relation $E(p) = c\left(p^2 + m^2c^2\right)^{\frac{1}{2}} - mc^2$, we find that

$$q(\boldsymbol{r};\varepsilon) = e\sum_{\Lambda}\left[\tilde{\chi}^{\dagger}_{\Lambda}(\boldsymbol{r};p)\tilde{\chi}_{\Lambda}(\boldsymbol{r};p)\right]_{p=[(\varepsilon/c)^2-(m_ec)^2]}^{1/2} \tag{18}$$

$$= e\sum_{Q',Q}\tilde{\boldsymbol{\Phi}}^{\dagger}_{Q}(\boldsymbol{r};\varepsilon)\tilde{\boldsymbol{\Phi}}_{Q'}(\boldsymbol{r};\varepsilon)\left[\mathbf{b}^{\dagger}(\varepsilon)\mathbf{b}(\varepsilon)\right]^{-1}_{Q',Q} \tag{19}$$

and similarly

$$m(r;\varepsilon) = \mu_{\text{Bohr}} \sum_{Q',Q} \tilde{\Phi}^{\dagger}_{Q}(r;\varepsilon)\beta\,\sigma\tilde{\Phi}_{\ Q'}(r;\varepsilon)\left[\mathbf{b}^{\dagger}(\varepsilon)\mathbf{b}(\varepsilon)\right]^{-1}_{Q',Q}. \tag{20}$$

These relations take a more familiar form when expressed in terms of the Z functions [26, 20]

$$\tilde{Z}_{\Lambda}(r) = \left(\pi\hbar^2c^2/2q\varepsilon\right)^{1/2}\tilde{\chi}_{\Lambda'}\,\mathbf{t}^{-1}_{\Lambda',\Lambda} \tag{21}$$

$$\lim_{r\to\infty}\tilde{Z}_{\Lambda}(r) = \left(\frac{2\pi\hbar^2c^2}{q\varepsilon}\right)^{1/2}\left(q\,\tilde{n}_{\Lambda} + \sum_{\Lambda'} K^{-1}_{\Lambda',\Lambda}\,\tilde{j}_{\Lambda'}\right).$$

Substituting equation (21) into equation (18), we find that

$$q(r;\varepsilon) = -e\frac{2\varepsilon}{\hbar^2c^2}\frac{1}{\pi}\operatorname{Im}\sum_{\Lambda',\Lambda}\tilde{Z}^{\dagger}_{\Lambda}(r;\varepsilon)\tilde{Z}_{\ \Lambda'}(r;\varepsilon)\,\mathbf{t}_{\ \Lambda',\Lambda}(\varepsilon)$$

$$m(r;\varepsilon) = -\mu_{\text{Bohr}}\frac{2\varepsilon}{\hbar^2c^2}\frac{1}{\pi}\operatorname{Im}\sum_{\Lambda',\Lambda}\tilde{Z}^{\dagger}_{\Lambda}(r;\varepsilon)\,\beta\sigma\,\tilde{Z}_{\ \Lambda'}(r;\varepsilon)\,\mathbf{t}_{\ \Lambda',\Lambda}(\varepsilon)$$

where we have used the identities

$$(\mathbf{t}^{\dagger}\mathbf{t}) = (\mathrm{i}/2q)(\mathbf{t} - \mathbf{t}^{\dagger})$$

$$\operatorname{Tr}\{(\mathbf{t} - \mathbf{t}^{\dagger})\,\tilde{Z}^{\dagger}\,\tilde{Z}\} = \operatorname{Tr}\{\tilde{Z}^{\dagger}\,\tilde{Z}\,\mathbf{t}\} - \left[\operatorname{Tr}\{\tilde{Z}^{\dagger}\,\tilde{Z}\,\mathbf{t}\}\right]^{*} = 2\operatorname{Im}\operatorname{Tr}\{\tilde{Z}^{\dagger}\,\tilde{Z}\,\mathbf{t}\}.$$

Note that when atomic units are used, $\lim_{c\to\infty}(2\varepsilon/\hbar^2c^2) = 1$.

These results can be generalized to the multiple-scattering case either by constructing the system's Green function from the scattering solutions or more directly from the secular equation of multiple-scattering theory [10, 27]. The required generalizations of the standard formulae [20] are

$$q^{i}(r_i;\varepsilon) = -e\frac{2\varepsilon}{\hbar^2c^2}\frac{1}{\pi}\operatorname{Im}\sum_{\Lambda',\Lambda}\tilde{Z}^{i\dagger}_{\Lambda}(r;\varepsilon)\tilde{Z}^{i}_{\Lambda'}(r;\varepsilon)\,\tau^{il}_{\Lambda',\Lambda}(\varepsilon)$$

$$m^{i}(r;\varepsilon) = -\mu_{\text{Bohr}}\frac{2\varepsilon}{\hbar^2c^2}\frac{1}{\pi}\operatorname{Im}\sum_{\Lambda',\Lambda}\tilde{Z}^{i\dagger}_{\Lambda}(r;\varepsilon)\beta\sigma\tilde{Z}^{i}_{\Lambda'}(r;\varepsilon)\tau^{ii}_{\Lambda',\Lambda}(\varepsilon)$$

where

$$\tau^{ij\,-1}_{\Lambda',\Lambda} = -\,\Omega^{-1}_{\text{BZ}}\int_{\text{BZ}}\left[\mathrm{i}q\,\delta_{\Lambda',\Lambda} - \mathbf{t}^{-1}_{\Lambda',\Lambda} + \mathbf{B}^{ij}_{\Lambda',\Lambda}(k,\varepsilon)\right]\exp\left[-\mathrm{i}k\cdot\left(R_i - R_j\right)\right]\mathrm{d}^3k \tag{22}$$

the superscripts label Wigner–Seitz cells, and the $B^{ij}_{\Lambda',\Lambda}(k,\varepsilon)$ are the usual relativistic structure constants for the lattice. Because the basis functions within the Wigner–Seitz cell are independent of the potential in the moon regions, the basis functions used in the above formulae can be identical to those used to calculate the t-matrix.

7. Results of implementing the full potential KKR theory

In order to illustrate the power of the above theory, we shall now report on a number of calculations for iron and silicon. In the first case we shall focus on the interaction between the local magnetic moment and the cubic crystal field. In the second case, we shall aim to demonstrate that our full-potential KKR theory can describe the highly directional sp^3 bonds in silicon with a relatively low value for L_{max}.

Unless stated otherwise, the results quoted below were obtained with $L_{max} = 2$. Relativistic units are used throughout, with the physical value of the speed of light c being *unity*. The aspherical electric scalar potential was in each case determined by a self-consistent linearized augmented plane wave (LAPW) calculation, using a code [28] generalized to cope with systems lacking inversion symmetry. As is well known, for iron the electric potential has (cubic) components in Y_4^0 and $Y_4^{4(C)}$; and Y_6^0 and $Y_6^{4(C)}$ while for silicon, there is an additional (tetrahedral) component in $Y_3^{2(S)}$ [29]. The spin-dependent potential used to obtain the results quoted for iron was taken from the literature [30]. We begin by displaying the effects of non-sphericity in the case of a single scatterer.

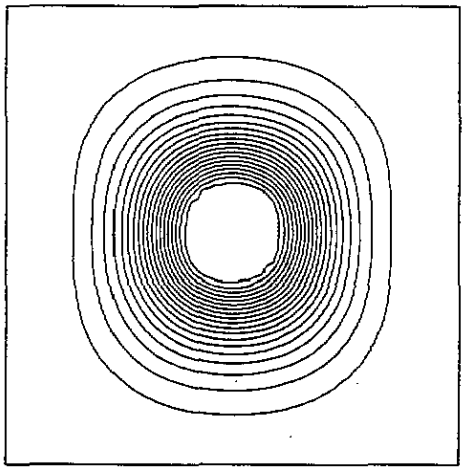

Figure 3. Log of charge density on the [110] plane for the warped muffin-tin iron potential, with its $l = 4$ component boosted tenfold. The core region has been removed.

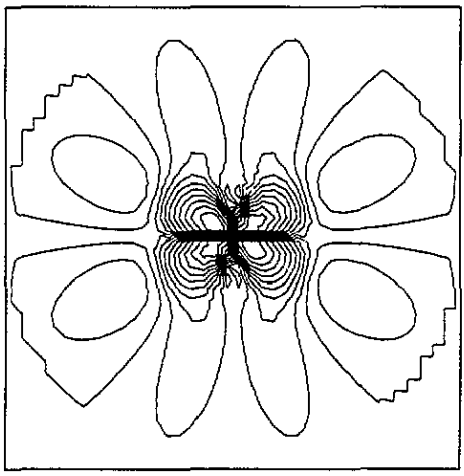

Figure 4. $\sinh^{-1} M_{[100]}$ on the [110] plane for the warped muffin-tin iron potential, with its $l = 4$ component boosted tenfold, and the magnetization along (001).

7.1. D-wave phase shifts for iron

A charge density plot for a warped muffin-tin iron potential, with the local magnetization aligned perpendicular to one face of the Wigner–Seitz cell, the (100) axis, is given in figure 3. The $l = 4$ component of the electric scalar potential is non-physical in that it has been boosted tenfold to illustrate the effect of asphericity. The peripheral charge distribution, though non-spherical, is smooth and has no lobes, indicating the absence of covalent bonding. It is slightly stretched out along the plot's y axis because the neighbouring atoms on this plane are further away from the central atom in this direction than the other.

The influence of the anisotropic scalar potential can be seen in figure 4, where the component of the magnetization density *perpendicular* to the imposed W direction is shown. The inverse hyperbolic sine of the magnetization is plotted to compress the large range of the plot. A substantial orthogonal magnetization can be seen in the core region.

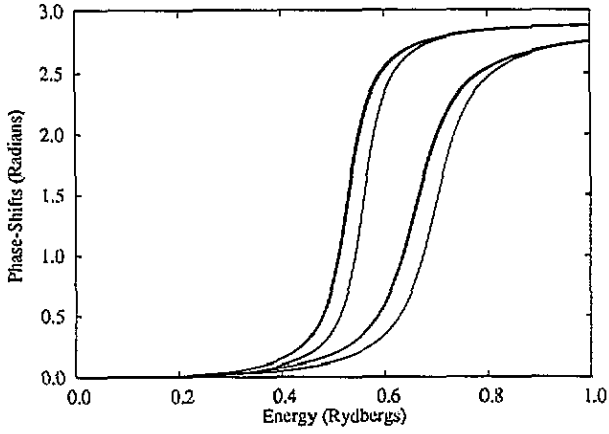

Figure 5. *D*-wave resonances for the warped muffin-tin iron potential.

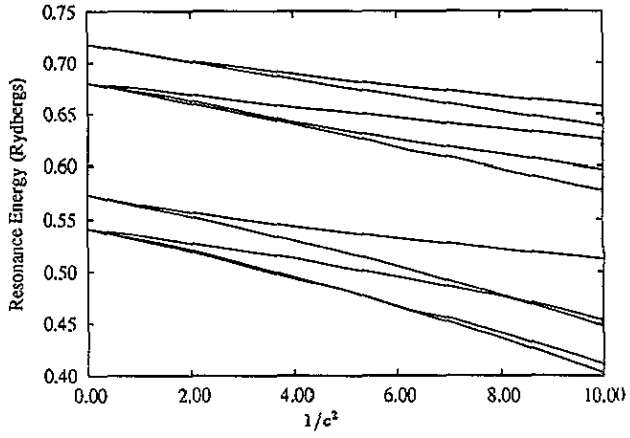

Figure 6. *D*-wave resonances versus $1/c^2$, for the warped muffin-tin iron potential. $c = 1$ corresponds to physical reality.

The *D*-like phase shifts (see discussion at equation (15)) for the above potential are given in figure 5. To illustrate the effects of relativity, the *D*-like resonance energies for the same potential are plotted against $1/c^2$ in figure 6. It is not easy to make sense of these data, as the effects of the anisotropic scalar potential and the spin-polarization $\boldsymbol{W} \cdot \boldsymbol{S}$, and relativistic $\boldsymbol{L} \cdot \boldsymbol{S}$ interactions are of similar magnitude. To clarify the situation, it is helpful to consider in turn first the three extreme cases where only one of these interactions is significant and then how these merge into each other. This can best be done by focusing

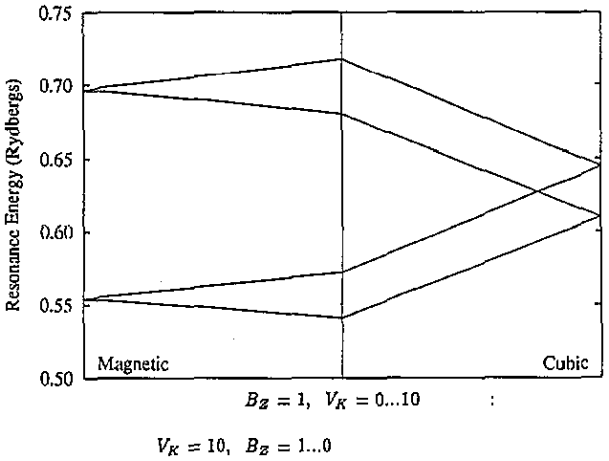

Figure 7. Iron D-wave resonances, non-relativistic case.

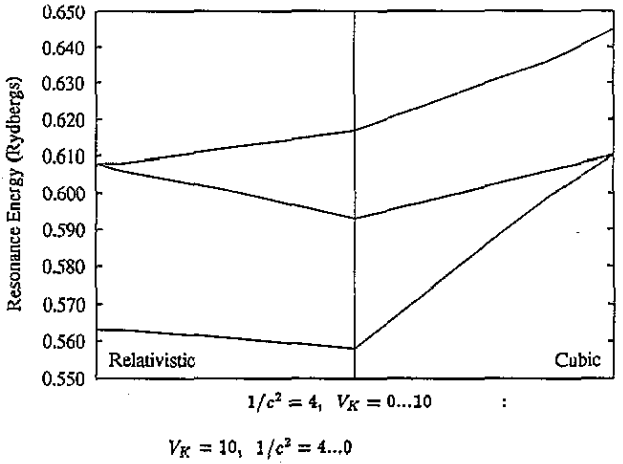

Figure 8. Iron D-wave resonances, non-magnetic case. $c = 1$ corresponds to physical reality.

on the segregation pattern of the D-like resonances as a function of the three interaction strengths.

Figure 7 relates to the non-relativistic case. On the left, the spin-polarization potential has its nominal value, and the anisotropic part of the electric scalar potential varies from zero to ten times nominal. On the right, the scalar potential is maintained at ten times its nominal value and the magnetization is reduced from its true value down to zero. The change over from the spin-up/spin-down pentuplets to the doubly degenerate cubic triplet Γ'_{25} and doublet Γ_{12} is clear. In the non-relativistic regime these two interactions are additive, spin being independent of orbital motion.

Figure 8 relates to the non-magnetic case. On the left, relativistic effects are maximized, with the speed of light set at 0.5, and the anisotropic electric potential varies from zero to ten times nominal. On the right the cubic anisotropy of the electric potential is maintained at its maximum value, and the speed of light is increased from 0.5 up to ∞. The change over

from the relativistic pattern of a $J = \frac{3}{2}$ quartet and $J = \frac{5}{2}$ hextuplet to the non-relativistic cubic degeneracies is clear. It is interesting to note that while the four resonances which on the right belong to the Γ_{12} irrep remain degenerate throughout, the six Γ'_{25} resonances split, one pair moving over to join with what was the Γ_{12} group, and so constituting the $J = \frac{5}{2}$ hextuplet on the left of the figure.

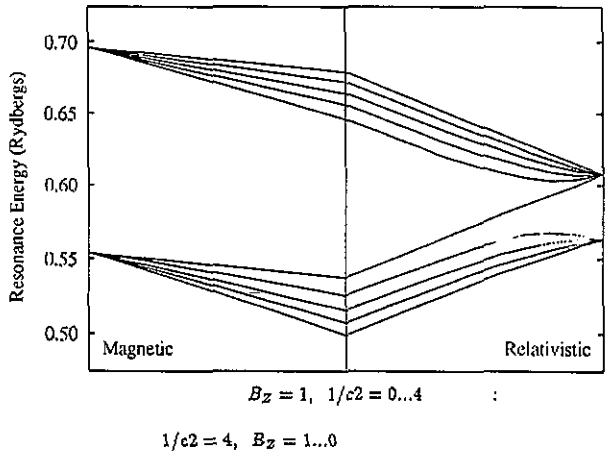

Figure 9. Iron D-wave resonances, isotropic electric potential case. $c = 1$ corresponds to physical reality.

Figure 9 relates to the isotropic scalar potential case [2]. On the left, the magnetization has its nominal value, and the speed of light varies from infinity down to half its true value. On the right, the speed of light is maintained at 0.5, and the magnetization is reduced from its nominal value down to zero. The change over from spin-up/spin-down splitting to the relativistic pattern of degeneracies is clear. The conflict between the propensity of the spin of each electron to align on the one hand with the imposed magnetization, and on the other with its own orbital motion is apparent.

7.2. Single-site magneto-crystalline anisotropy for iron

To gain further insight into the coupling of the local magnetic moment to the crystal field, we have studied the magneto-crystalline anisotropy of a single iron potential well. We found the Fermi level and electronic internal energy U_E of the single-site system with the magnetization oriented in the [001], [110] and [111] directions by using the Friedel sum, as derived in appendix B, for the spin-dependent density of states. In the non-relativistic limit, a magnetic field only interacts with the electron spins, which are themselves entirely decoupled from the crystal field. The magneto-crystalline anisotropy is in this limit identically zero, and the effect revealed as essentially relativistic.

In figure 10 $U_E[001] - U_E[111]$ and $U_E[001] - U_E[110]$ are plotted against $1/c^2$, for a warped muffin-tin iron potential. $U_E[001] - U_E[111]$ starts slightly positive, becomes negative (falling to a minimum for $c = 0.45$) and then rises steeply for lower values. Taking these calculations at face value, at intermediate values of c, the [001] magnetization results in the lowest internal energy, and the [111] the highest; so the easy axis might be expected to lie along [100]. On the other hand, in both the extreme relativistic and non-relativistic limits,

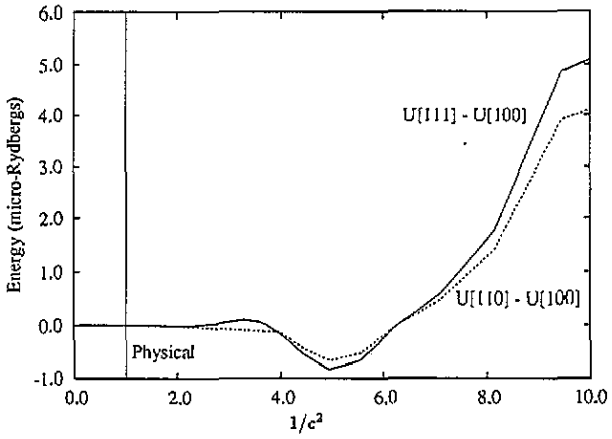

Figure 10. Single-site component of the magneto-crystalline anisotropy for the warped muffin-tin iron potential. $c = 1$ corresponds to physical reality.

the [111] orientation is the least energetic and the [100] orientation the most energetic, and the easy axis should then lie along [111]. However, for $c = 1$, the single-site contribution to the anisotropy energy is truly negligible [31]. Evidently, such calculations would be more interesting if carried out for bulk materials. Moreover, realistic quantitative calculations certainly require the development of a fully self-consistent procedure.

7.3. Magnetic anisotropies in the band structure of iron

The $L_{max} = 2$ spin-polarized band structure for the warped muffin-tin iron potential in the region of ε_F and along the lines K (1/2 , 1/2 , 0) $-\Gamma$ and $\Gamma-$ L (1/2 , 1/2 , 1/2) is given in figure 11. Bands are given for the magnetization directed both along the [001] and [111] directions. In this region of the Brillouin zone the D-wave bands are very complicated, being first split by the large exchange splitting $\boldsymbol{W} \cdot \boldsymbol{S}$ term and then distorted by the mutual repulsion of those bands belonging to the same irreps of the space group that are brought into proximity by the $\boldsymbol{W} \cdot \boldsymbol{S}$ shifts. The set of bands featured in figure 11 have almost pure spin character, but some J-character is retained, and this is the cause of the splittings evident where they cross the Γ point. The impact of the cubic space group is clearly seen in the approximate triplet/doublet segregation of these five bands, the lifting of this degeneracy at the milliRydberg level is due to angular-momentum orientation. Because it changes the space group, rotating the magnetization alters which bands can cross each other (see for example the behaviour at 0.662 Ryd and 0.626 Ryd, half-way between K and Γ) as well as more generally changing the magnitude of the band repulsions.

A comparison of the upper (triplet) set of bands at the Γ point for the isotropic muffin-tin and warped muffin-tin cases is given in figure 12. While the anisotropy of the cell potential is seen to shift the bands bodily by about 2 mRyd, it does not significantly change the *difference* in band energies for the two orientations of magnetization. This is not surprising, because as has already been remarked, the latter effect is largely attributable to $\boldsymbol{W} \cdot \boldsymbol{J}$. It might appear, therefore, that the use of a warped muffin-tin cell potential in a calculation of the magneto-crystalline anisotropy of iron would give essentially the same result as would be obtained with an isotropic muffin-tin cell potential. However, because the true magneto crystalline anisotropy is in the region of only 20 μRyd, it is still not clear that the cell potential anisotropy has a negligible role in determining its exact value [31].

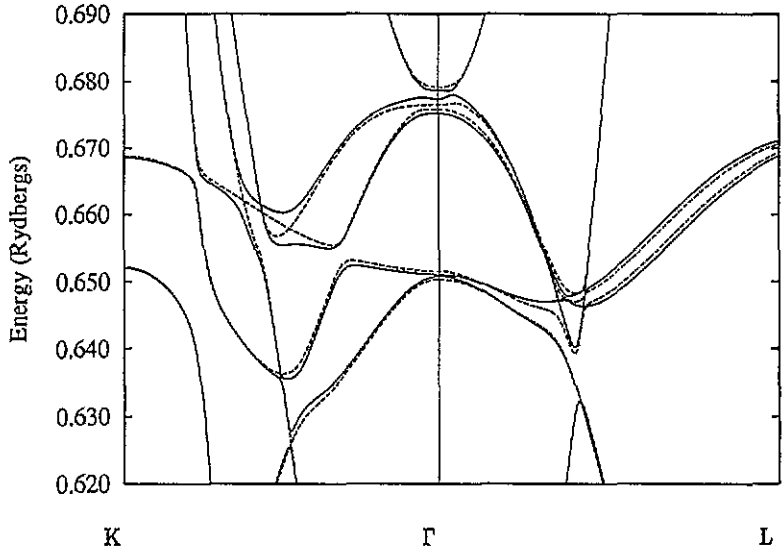

Figure 11. $L_{max} = 2$ D-wave bands for the warped muffin-tin iron potential. The full curves are for the magnetization along [111] and the broken curves for the magnetization along [001].

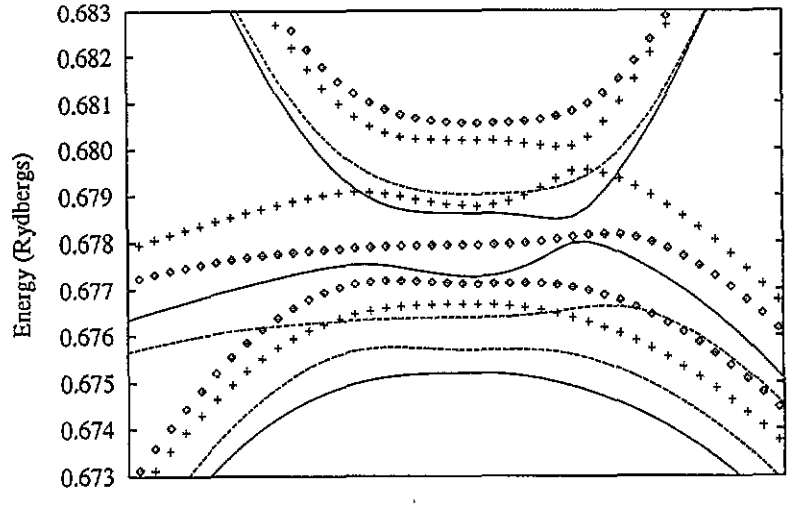

Figure 12. $L_{max} = 2$ D-wave bands for the warped muffin-tin iron potential in the region of the Γ point (curves), compared to the isotropic case (points).

7.4. The band structure of silicon

Silicon has one of the most open lattices encountered in solid-state theory. The radius of its Wigner–Seitz circumsphere is in fact equal to its nearest-neighbour separation. It has long been thought impractical to apply multiple-scattering techniques in such circumstances without the use of auxiliary empty spheres [32]. Our results show this judgement to have been unduly pessimistic.

In principle, our calculations should agree with the results obtained with the self-

consistent LAPW code, because the potential used is identical. *Exact* agreement was not expected because the LAPW uses a linear approximation technique and becomes less accurate at higher energies.

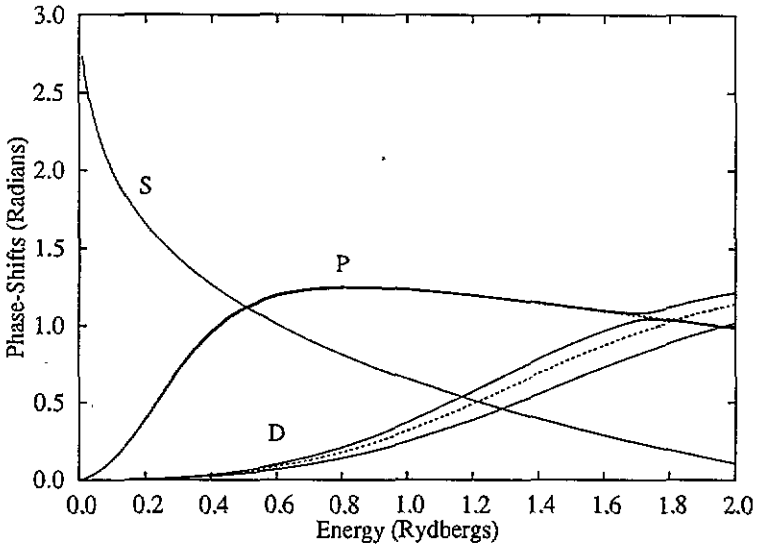

Figure 13. Phase shifts for the warped muffin-tin silicon potential, (with its $l = 4$ part boosted tenfold). Results for the isotropic case are given as broken curves, for comparison.

The unit cell of the silicon lattice contains two atoms. The **S**-matrix of the second can be obtained from that of the first by either reflecting it in the xy plane or rotating it about the z axis by one quarter revolution. The S-, P- and D-like phase shifts for a warped muffin-tin silicon potential are given in figure 13. To illustrate the effect of asphericity, the $l = 4$ component of the anisotropy has been increased tenfold. The $j = \frac{3}{2}$ and $j = 1/2$ P-wave splitting can hardly be seen, because relativistic effects are so small. The phase shifts are seen to deviate significantly from those of the isotropic case only where two waves belonging to the same irreducible representation of the symmetry group characteristic of the scattering potential have similar phase shifts; and in particular when these would be identical in the absence of the anisotropy. In the energy range of interest, this condition is only met for the P and D-waves, and then only substantially above ε_F. Even so, for energies in the region of ε_F (and hence the band gap), the P- and D-like partial waves are of somewhat mixed character. This shows up clearly in the charge density, figure 14, calculated using (19) and (20). The regions of increased electron density are remnants of the covalent bond charge that build up between nearest neighbours in crystalline silicon.

The **S**-matrix of a space-filling potential (figures 15 and 16) was evaluated on the Wigner–Seitz circumsphere as described in section 5, above. The generalized phase shifts for $L_{max} = 2$ are given as figure 17. The phase shifts for the isotropic muffin-tin potential are plotted as broken curves on the same graph for comparison. Although no anisotropic components have been boosted, the D-like phase shifts show significant cubic splitting. This is due to the potential in the interstitial regions within silicon's open lattice, which plays a critical role in defining the element's band structure. The second (and dominant) effect, however, is the peaking of the P-wave resonance and the reduction of its energy

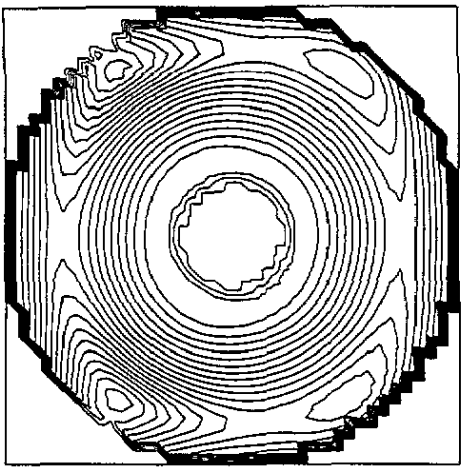

Figure 14. Log of charge density on the [110] plane for the warped muffin-tin silicon potential, with its $l = 4$ part boosted tenfold. The core region has been removed.

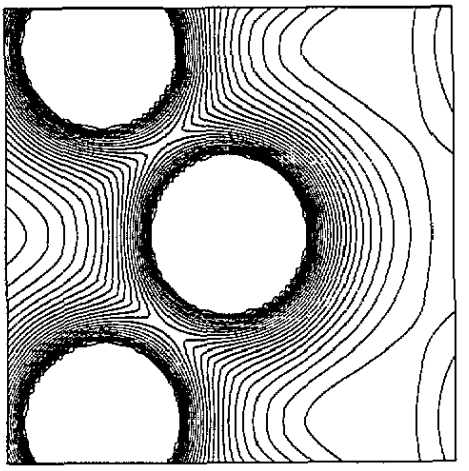

Figure 15. The space-filling silicon potential on the [110] plane, constructed within each Wigner–Seitz cell from an isotropic component together with others proportional to $Y_3^{2(S)}$, Y_4^0, $Y_4^{4(C)}$, Y_6^0 and $Y_6^{4(C)}$. The core region has been removed.

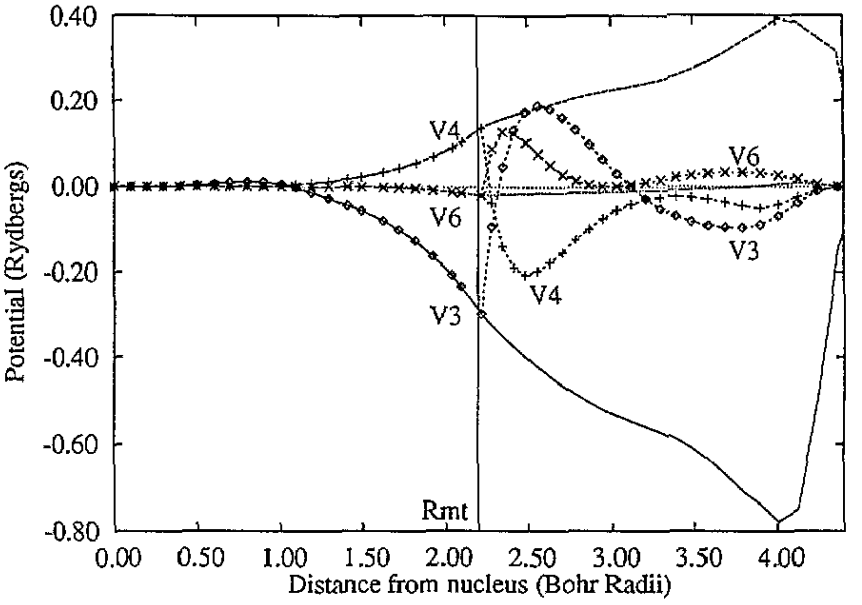

Figure 16. V_3, V_4 and V_6 anisotropic potential components for the space-filling silicon potential. Values for the analytically continued potential which gives the best fit within Γ_{WS} are given as curves. Values representing the potential when abruptly truncated at Γ_{WS}, as used in our calculations, are given as points.

by about 0.2 Ryd. These effects are largely attributable to the additional isotropic potential component now present between the muffin-tin and Wigner–Seitz circumsphere. The *S*-

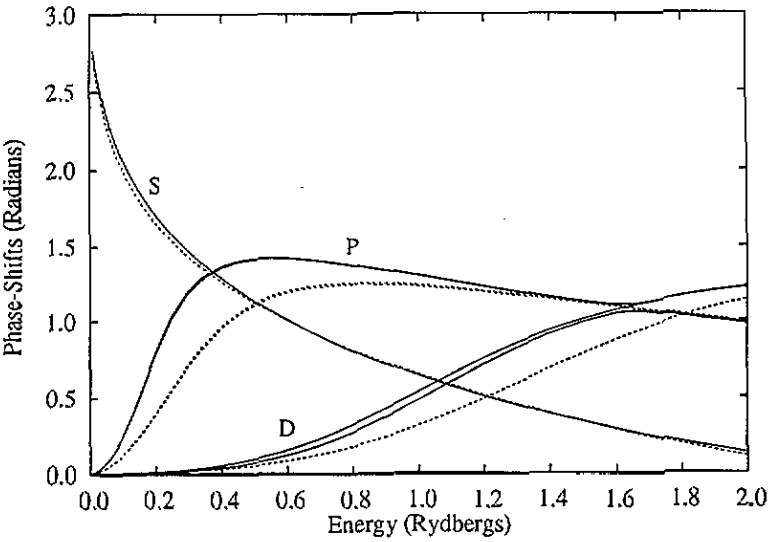

Figure 17. Phase shifts for the space-filling silicon potential, with $L_{max} = 2$. Results for the isotropic muffin-tin potential are shown as broken curves, for comparison.

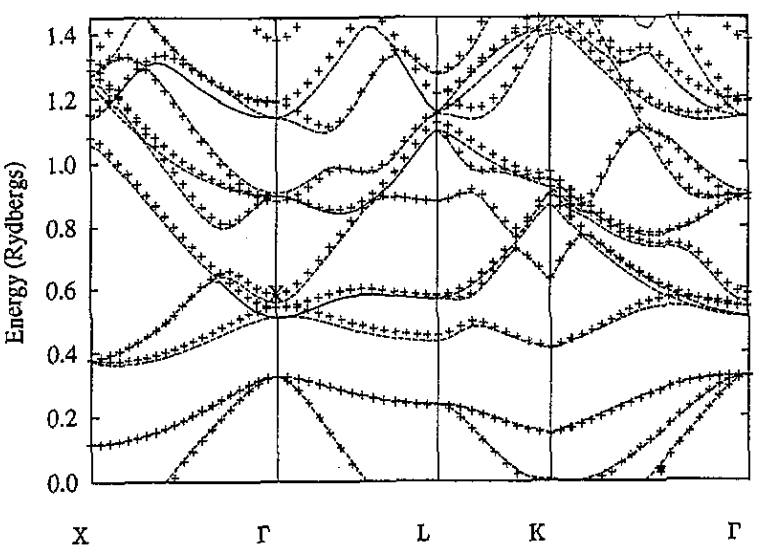

Figure 18. *P*-, *D*- and *F*-wave components of the *P*- and *D*-like eigenvectors of the S-matrix for the space-filling silicon potential, with $L_{max} = 3$.

and *P*-like phase shifts are not affected to first order by any tetrahedral or cubic aspherical components, and for $L_{max} = 2$, the *S*-like phase-shift is unperturbed to *all* orders.

However, a first-order mixing of *P* and *D* waves *does* occur for $L_{max} = 3$ via the $l = 3$ tetrahedral potential component, see figure 18. This plays a significant role in defining the

band structure, though *not* the phase shifts. In particular, while the P-like phase shift is affected only quadratically, the electronic bands depend linearly on this anisotropy. This is because the tetrahedral concentration of bond charge is essentially built up by multiple scattering from the lattice, and so is *zeroth order* in the atomic anisotropy. The latter is, however, aligned with the anisotropy of the charge distribution and so shifts the bands in first order. This effect is represented in the KKR formalism for the tetrahedral silicon lattice by appropriate off-site diagonal terms in the structure constant matrix.

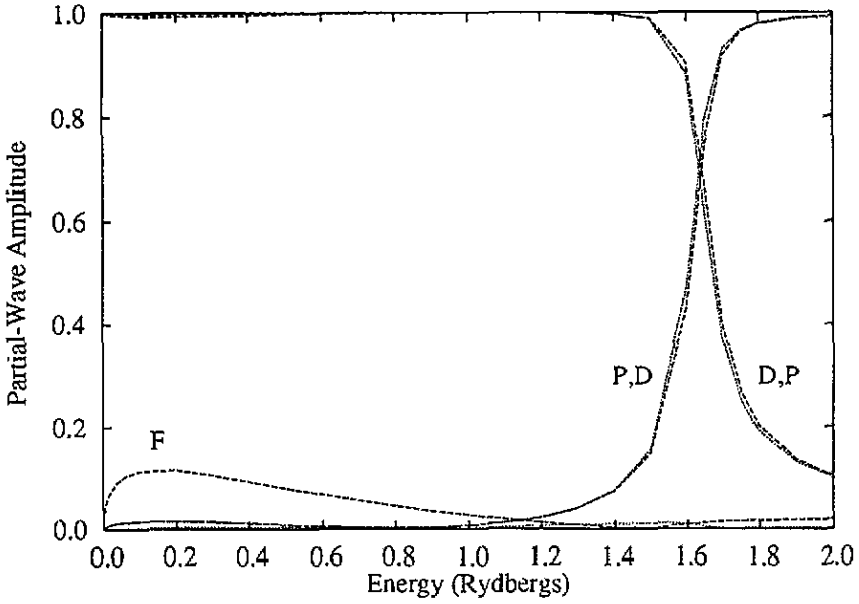

Figure 19. KKR (L_{max} = 2) results (points) versus LAPW results (curves) for the space-filling silicon potential.

Figure 19 shows the agreement of our full-potential KKR results for an L_{max} of two with our LAPW results for the same potential. The most notable effect is that an (indirect) band gap has opened up. A second effect can be seen in the form of the conduction bands between the Γ and X points. These are made up of a non-degenerate S-wave antibonding band (marked X at [Γ, 0.58 Ryd]) and a triply degenerate P-wave antibonding band, which away from Γ is split by the reduced symmetry of the space group into a doubly degenerate band and a non-degenerate band. In both the muffin-tin cases, the S-wave band is slightly lower in energy than the P-wave band at Γ, whereas in the space-filling case it lies at a higher energy. This effect is to be seen in both the KKR and LAPW results.

Calculations with $L_{max} > 2$ were complicated by the fact that the higher-angular-momentum eigenphases have a tendency to pass through zero. This causes the inverse **t**-matrix to become singular, and led our KKR code to produce spurious bands. This difficulty was overcome by accurately locating the poles of $\mathbf{t}^{-1}$, then eliminating the resulting k-independent false bands [33] by discounting reversals of the polarity of KKR eigenvalues occurring at these energies. For this scheme to work, it is crucial to employ an accurate interpolation method when constructing $\mathbf{t}^{-1}$ for energies other than those at which it is calculated by coupled radial integration. We found that constructing the matrices from linearly interpolated eigenvectors and eigenphases (both of which are very smooth functions of energy) was satisfactory, as long as care was taken to preserve the Hermitian character of $\mathbf{t}^{-1}$.

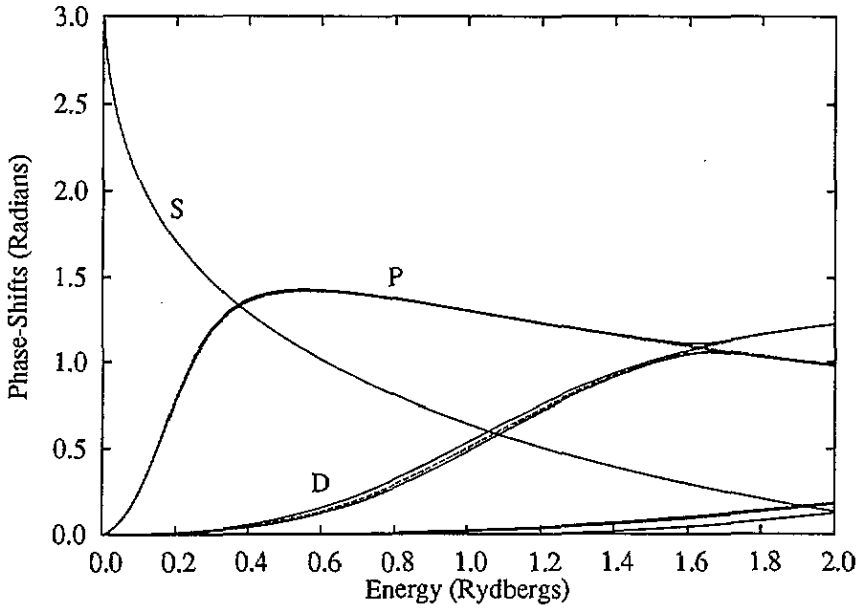

Figure 20. Phase shifts for the space-filling silicon potential, with $L_{max} = 3$. Results for the isotropic potential component alone are shown as broken curves, for comparison.

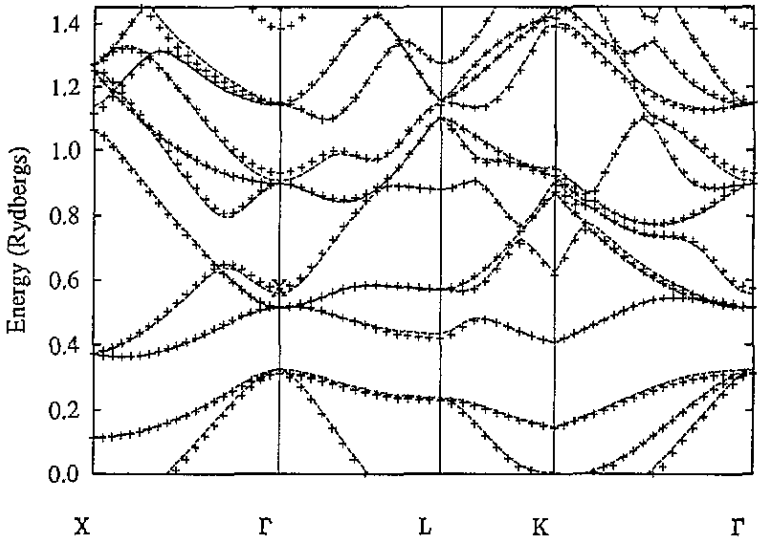

Figure 21. KKR ($L_{max} = 3$) results (points) versus LAPW results (curves) for the space-filling silicon potential.

Increasing L_{max} to three changed the phase shifts only slightly (figure 20), and improved the band structure results at higher energies (figure 21) but introduced no new features. It is inevitable that $L_{max} = 3$ will give anomalous results for the S-wave antibonding band (again marked X). The wave function of any covalent antibonding band has a low amplitude

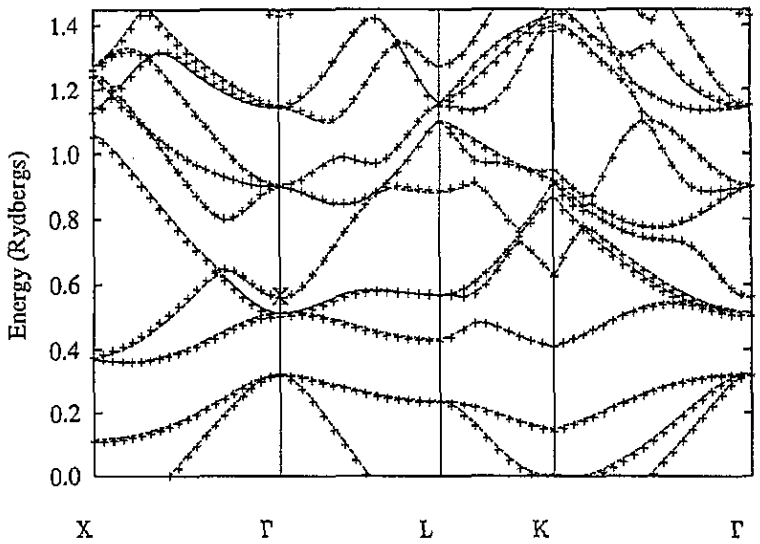

Figure 22. KKR ($L_{max} = 4$) results (points) versus LAPW results (curves) for the space-filling silicon potential.

in the bond-charge regions, where the V_3 and V_4 add, but a high amplitude in the interstitial regions, where the V_3 and V_4 tend to cancel. Now, V_4 only affects S-wave bands to first-order when $L_{max} = 4$, at which point it couples in G waves. Hence, limiting L_{max} to three means that of all the anisotropic potential components, only V_3 has a first-order effect on the energy of this band at the Γ point. The resulting neglect of V_4 shifts the S-wave antibonding band up in energy, because its wave function will be affected by the positive lobes of the V_3 (which lie in the interstitial regions) much more than by their negative counterparts (which lie in the regions of bond charge). Increasing L_{max} to four (figure 22) allows V_4 to have a first-order effect on the S-wave antibonding band's energy, and brings it back to its position in the $L_{max} = 2$ case where *all* anisotropic potentials are ignored as far as this band is concerned.

8. Conclusions

We have developed an efficient method for calculating the fully relativistic spin-polarized scattering amplitudes for a non-spherically symmetric potential to be used in KKR band-theory calculations. We have discussed L_{max} truncation of the Hamiltonian, and justified our use of this approximate procedure. Moreover, we have argued for the validity of full-potential KKR theory, and that the **t**-matrix should be evaluated on the Wigner–Seitz circumsphere for an approximate cell potential. We have illustrated our method with relativistic calculations for iron, and with calculations for silicon that avoid using non-atomic 'empty spheres' and require an L_{max} of at most four. The excellent agreement between our LAPW and KKR $L_{max} = 4$ results even at higher energies tends to legitimize *both* calculation schemes.

It is most satisfactory that a substantially complete description of the dynamics of electrons in such an open structure can now be given in terms of one *atomic* **s**-matrix per site, and especially one with such a low angular-momentum cut-off. The absence of

near-field corrections in this most difficult of cases constitutes a strong practical argument against their existence in any circumstances whatever.

At all stages in our analysis, we have maintained the separation between the dynamics of the atomic scattering problem and the geometric effects of the crystal lattice. We believe that this approach facilitates physical insight into the electronic properties of whatever system the method is applied to. In particular, we expect the illuminating role still played by the single-site generalized phase shifts (now augmented by their corresponding eigenvectors) will prove fruitful in future work.

Acknowledgments

S C Lovatt would like to thank P Miller, P Boasman, J Staunton and P Strange, for many helpful discussions and encouragement, and B Drittler for providing him with a copy of his PhD thesis. This work was partly financed by SERC award 90101004.

Appendix A. The Wronskian divergence theorem

Consider the divergence of the local contribution to the matrix element of α, the relativistic flux-operator:

$$\nabla \cdot \left(\tilde{\phi}^\dagger \alpha \tilde{\psi}\right) = \tilde{\phi}^\dagger \alpha \cdot \left[\nabla \tilde{\psi}\right] + \left[\tilde{\psi}^\dagger \alpha \cdot \nabla \tilde{\phi}\right]^* = (\mathrm{i}/\hbar c)(\tilde{\phi}^\dagger \mathbf{H}_D \tilde{\psi} - [\tilde{\psi}^\dagger \mathbf{H}_D \tilde{\phi}]^*) \tag{A1}$$

for every point in space, where $\mathbf{H}_D$ is the Dirac Hamiltonian for some real potential.

If $\tilde{\psi}$ is an RHS eigenfunction of $\mathbf{H}_D$ with energy ε, and $\tilde{\phi}$ an RHS eigenfunction of $\mathbf{H}_D$, but with energy ε^*, then the following identity holds:

$$\left[\tilde{\psi}^\dagger \mathbf{H}_D \tilde{\phi}\right]^* = \left[\mathbf{H}_D \tilde{\phi}\right]^\dagger \tilde{\psi} = \left[\varepsilon^* \tilde{\phi}\right]^\dagger \tilde{\psi} = \varepsilon \tilde{\phi}^\dagger \tilde{\phi} = \tilde{\phi}^\dagger \mathbf{H}_D \tilde{\psi}.$$

Thus:

$$\nabla \cdot \left(\tilde{\phi}^\dagger \alpha \tilde{\psi}\right) = 0 \tag{A2}$$

which constitutes the local version of the Wronskian divergence theorem. In conjunction with Green's theorem this implies that any closed surface integral of $\tilde{\phi}^\dagger \alpha \tilde{\psi}$ is zero if these functions are solutions of the wave equation with the same potential, and are regular within the surface of integration. Moreover it implies that an integral over a general surface Γ can be distorted into an integral over a sphere, $\mathcal{S}$, of radius ρ.

$$\begin{aligned} W_\Gamma\left[\tilde{\Phi}_{Q_1}; \tilde{\Phi}_{Q_2}\right] &= \mathrm{i}\rho^2 \sum_\Lambda \bar{\mathsf{R}}^\dagger_{\Lambda,Q_1}(\rho)\sigma_y \bar{\mathsf{R}}_{\Lambda,Q_2}(\rho) \\ &= \mathrm{i}\rho^2 \sum_\Lambda [\bar{\mathsf{R}}^*_{\Lambda,Q_1;1}(\rho)\bar{\mathsf{R}}_{\Lambda,Q_2;2}(\rho) - \bar{\mathsf{R}}^*_{\Lambda,Q_1;2}(\rho)\,\bar{\mathsf{R}}_{\Lambda,Q_2;1}(\rho)]. \end{aligned} \tag{A3}$$

This means that a Wronskian taken between any two of the regular basis functions will be zero, for all values of ρ, because of the boundary conditions satisfied by the values of $\tilde{\Phi}_Q$ at the origin, which trivially ensure that

$$\lim_{\rho \to 0} W_{\mathcal{S}}[\tilde{\Phi}_{Q_1}; \tilde{\Phi}_{Q_2}] = 0.$$

Beyond Γ_{WS}, the $\tilde{\Phi}_Q$ become sums of free-space solutions, and $W[\tilde{\Phi}_{Q_1}; \tilde{\Phi}_{Q_2}]$ can be written in terms of the **a** and **b** matrices and W_0:

$$\sum_{\Lambda} W\left[\mathbf{a}^*_{\Lambda,Q_1}\tilde{h}^-_{\Lambda'} + \mathbf{b}^*_{\Lambda,Q_1}\tilde{h}^+_{\Lambda'}; \mathbf{a}_{\Lambda,Q_2}\tilde{h}^+_{\Lambda'} + \mathbf{b}_{\Lambda,Q_2}\tilde{h}^-_{\Lambda'}\right] = 0 \qquad \forall\, Q_1, Q_2$$

$$\sum_{\Lambda} \left(\mathbf{a}^*_{\Lambda,Q_1}\mathbf{a}_{\Lambda,Q_2} - \mathbf{b}^*_{\Lambda,Q_1}\mathbf{b}_{\Lambda,Q_2}\right) W_0 = 0$$

and hence

$$\mathbf{a}^\dagger\mathbf{a} = \mathbf{b}^\dagger\mathbf{b}$$

consequently, using equation (10)

$$\mathbf{s}^\dagger = \mathbf{s}^{-1} \tag{A4}$$

and the *Wronskian divergence theorem* is seen to imply the unitarity of the **s**-matrix. This is not surprising as both conditions represent flux conservation.

A version of the optical theorem also follows immediately from the unitarity of the **s**-matrix.

$$\mathrm{Tr\ Im}\{\mathbf{t}\} = -\mathrm{i}\tfrac{1}{2}\mathrm{Tr}\{\mathbf{t} - \mathbf{t}^\dagger\} = -\mathrm{i}q\,\mathrm{Tr}\{\mathbf{t}^\dagger\mathbf{t}\}. \tag{A5}$$

This version of the optical theorem relates to the *trace* of the **t**-matrix rather than individual angular-momentum channels because of the inter-channel scattering introduced by an anisotropic potential. Of course in the basis that diagonalizes **t**, all the standard results of isotropic scattering theory can be recovered.

Appendix B. The Friedel sum

It is of interest to derive, in the present more general context, the well known Friedel sum [34]. An earlier non-relativistic treatment of the anisotropic case is to be found in [6]. Clearly, the density of states of a system is given by

$$n(\varepsilon) = \int_\infty \langle \boldsymbol{r}|\delta(\varepsilon - H)|\boldsymbol{r}\rangle\ \mathrm{d}^3r = \sum_{Q',Q}\left[\mathbf{b}(\varepsilon)^\dagger\mathbf{b}(\varepsilon)\right]^{-1}_{Q',Q}\int_\infty \tilde{\Phi}^\dagger_Q(\boldsymbol{r};\varepsilon)\tilde{\Phi}_{Q'}(\boldsymbol{r};\varepsilon)\,\mathrm{d}^3r. \tag{B1}$$

Defining

$$\mathbf{F}_{Q',Q} = \int_\infty \tilde{\Phi}^\dagger_{Q'}(\boldsymbol{r};\varepsilon)\,\tilde{\Phi}_Q(\boldsymbol{r};\varepsilon)\,\mathrm{d}^3r \tag{B2}$$

equation (B1) becomes

$$n(\varepsilon) = \mathrm{Tr}\left[\mathbf{b}\,\mathbf{F}^{-1}\,\mathbf{b}^\dagger\right]^{-1}. \tag{B3}$$

The essence of Friedel's famous result is a strikingly simple expression for $\mathbf{F}_{Q',Q}$ in terms of the scattering phase shifts $\{\delta_l(\varepsilon)\}$ describing a spherically symmetric, non-relativistic scatterer. In what follows, we extend this result to an aspherical relativistic scattering centre. To begin with, we note that $\mathbf{F}_{Q',Q}$ can be re-expressed in terms of the Wronskian of one radial solution with the energy derivative of the other.

We follow Friedel's argument and define $\tilde{\psi}$ and $\tilde{\phi}$ by the relations $\mathbf{H}_\mathcal{D}\tilde{\psi} = \varepsilon\tilde{\psi}$ and $\mathbf{H}_\mathcal{D}\tilde{\phi} = \varepsilon^*\tilde{\phi}$, where $\mathbf{H}_\mathcal{D}$ is the Dirac Hamiltonian for some real potential. Then,

by differentiating the first of these expressions with respect to the eigenvalue of $\tilde{\psi}$, and premultiplying by $\tilde{\phi}^\dagger$, it is easy to show that

$$\tilde{\phi}^\dagger \mathbf{H}_\mathcal{D} \frac{\mathrm{d}}{\mathrm{d}\varepsilon}\tilde{\psi} = \varepsilon \tilde{\phi}^\dagger \left(\frac{\mathrm{d}}{\mathrm{d}\varepsilon}\tilde{\psi} \right) + \tilde{\phi}^\dagger \tilde{\psi}$$

moreover

$$\left(\frac{\mathrm{d}}{\mathrm{d}\varepsilon}\tilde{\psi}^\dagger \right) H \, \tilde{\phi} = \varepsilon^* \left(\tilde{\phi}^\dagger \frac{\mathrm{d}}{\mathrm{d}\varepsilon}\tilde{\psi} \right)^*$$

and subtracting

$$\tilde{\phi}^\dagger \tilde{\psi} = \tilde{\phi}^\dagger \mathbf{H}_\mathcal{D} \frac{\mathrm{d}}{\mathrm{d}\varepsilon}\tilde{\psi} - \left[\left(\frac{\mathrm{d}}{\mathrm{d}\varepsilon}\tilde{\psi}^\dagger \right) \mathbf{H}_\mathcal{D} \tilde{\phi} \right]^* .$$

Substituting this into equation (A1)

$$\boldsymbol{\nabla} \cdot \left(\tilde{\phi}^\dagger \boldsymbol{\alpha} \frac{\mathrm{d}}{\mathrm{d}\varepsilon}\tilde{\psi} \right) = \frac{\mathrm{i}}{\hbar c} \phi^\dagger \psi .$$

Substituting this into equation (B2), and using Green's theorem

$$F_{Q',Q}(R) = -\mathrm{i}\hbar c \left[r^2 \int_{4\pi} \tilde{\boldsymbol{\Phi}}^\dagger_{Q}(\boldsymbol{r}) \boldsymbol{\alpha} \frac{\mathrm{d}}{\mathrm{d}\varepsilon} \tilde{\boldsymbol{\Phi}}_{Q}(\boldsymbol{r}) \cdot \mathrm{d}^2\hat{\boldsymbol{r}} \right]_{r=0}^{r=R} .$$

For large ρ and in the absence of a potential, it can be shown that

$$W_S \left[\tilde{\boldsymbol{\Phi}}_{Q}; \frac{\mathrm{d}}{\mathrm{d}\varepsilon}\tilde{\boldsymbol{\Phi}}_{Q} \right] = \frac{1}{\hbar c} \left[\frac{\rho}{\pi} \frac{\mathrm{d}q}{\mathrm{d}\varepsilon} \right] \left[1 + \frac{m_e c^2}{2\varepsilon q \rho} \sin(2q\rho + \pi l) \right].$$

Now, we consider the change in $n(\varepsilon)$ due to the scattering potential V as $\rho \to \infty$

$$\delta n(\varepsilon; [V]) = n(\varepsilon; [V]) - n(\varepsilon; [0]).$$

After further algebra, we find that

$$\delta n(\varepsilon; [V]) = \hbar c \lim_{R \to \infty} W_0 \, \mathrm{Tr} \left\{ \left(\mathbf{s}^{-1} \frac{\mathrm{d}}{\mathrm{d}\varepsilon}\mathbf{a} - \frac{\mathrm{d}}{\mathrm{d}\varepsilon}\mathbf{b} \right) \mathbf{b}^{-1} \right\}.$$

Surprisingly, this formula can be further simplified as follows

$$\delta n(\varepsilon) = -\frac{\mathrm{i}}{2\pi} \mathrm{Tr} \left\{ \mathbf{s}^{-1} \frac{\mathrm{d}}{\mathrm{d}\varepsilon}\mathbf{s} \right\} = -\frac{\mathrm{i}}{2\pi} \mathrm{Tr} \left\{ \frac{\mathrm{d}}{\mathrm{d}\varepsilon} \ln(\mathbf{s}) \right\} = \frac{1}{\pi} \sum_\nu \frac{\mathrm{d}}{\mathrm{d}\varepsilon}\delta_\nu(\varepsilon)$$

$$\delta N(\varepsilon; [V]) = \frac{1}{\pi} \sum_\nu \delta_\nu(\varepsilon)$$

where $N(\varepsilon)$ is the integrated density of states, $\int^\varepsilon \delta n(\varepsilon')\mathrm{d}\varepsilon'$. This is Friedel's original result, except that the generalized phase shifts, which are equal to half the eigenphases of the **s**-matrix, are involved.

References

[1] Korringa J 1947 *Physica* **13** 392
Kohn W and Rostoker N 1954 *Phys. Rev.* **94** 1111
[2] Strange P, Staunton J B and Gyorffy B L 1984 *J. Phys. C: Solid State Phys.* **17** 3355
[3] Feder R, Rosinskey F and Ackermann B 1983 *Z. Phys.* B **52** 31
[4] Drittler B, Weinert M, Zeller R and Dederichs P H 1990 *Phys. Rev.* B **42** 9336
[5] Drittler B, Weinert M, Zeller R and Dederichs P H 1991 *Solid State Commun.* **79** 31
[6] Drittler B 1991 *PhD Thesis* Aachen University
[7] Krewer J W and Feder R 1991 *Physica* B **172** 135
[8] Gonis A, Zhang X G and Nicholson D M 1989 *Phys. Rev.* B **38** 3564; *Phys. Rev.* B **40** 947
[9] Nesbet R K 1989 *Phys. Rev.* B **41** 4948
[10] Gonis A, Butler W H and Zhang X G 1991 *Mater. Res. Soc. Symp. Proc.* **253** 159
[11] Butler W H, Zhang X G and Gonis A 1992 *Mater. Res. Soc. Symp. Proc.* **253** 205
[12] Tamura E 1992 *Phys. Rev.* B **45** 3271
[13] Ginatempo B and Gyorffy B L 1990 *J. Phys.: Condens. Matter* **2** 5233
Gyorffy B L 1992 *Mater. Res. Soc. Symp. Proc.* **253** 173
[14] MacDonald A H and Vosko S H 1979 *J. Phys. C: Solid State Phys.* **12** L845
[15] Gordon W 1927 *Z. Phys.* **50** 630
[16] Rose M E 1961 *Relativistic Electron Theory* (New York: Wiley)
[17] Ebert H and Gyorffy B L 1988 *J. Phys. F: Met. Phys.* **18** 451
[18] Loucks T L 1967 *The Augmented Plane Wave Method* (New York: Benjamin)
[19] Schiff L I 1968 *Quantum Mechanics* (New York: McGraw-Hill)
[20] Weinberger P 1990 *Electron Scattering Theory for Ordered and Disordered Matter* (Oxford: Clarendon)
[21] Brown R G and Ciftan M 1983 *Phys. Rev.* B **27** 4564; 1985 *Phys. Rev.* B **32** 3454; 1986 *Phys. Rev.* B **33** 7937; 1992 *Mater. Res. Soc. Symp. Proc.* **253** 173
[22] Faulkner J S 1979 *Phys. Rev.* B **19** 6186; 1986 *Phys. Rev.* B **34** 5931
[23] Staunton J, Gyorffy B L and Weinburger P 1980 *J. Phys. F: Met. Phys.* **10** 2665
[24] Tamura E 1992 *Mater. Res. Soc. Symp. Proc.* **253** 347
[25] Roman P 1965 *Advanced Quantum Theory* (Reading, MA: Addison-Wesley)
[26] Faulkner J S 1982 *Prog. Mater. Sci.* **27** 1
[27] Butler W H and Nesbet R K 1990 *Phys. Rev.* B **42** 1518
[28] Blaha P, Schwarz K, Sorantin P and Trickey S B 1990 *Comput. Phys. Commun.* **59** 399
[29] Altmann S L and Cracknell A P 1965 *Rev. Mod. Phys.* **11** 19
[30] Moruzzi V L, Janak J F and Williams A R 1978 *Calculated Electronic Properties of Metals* (Oxford: Pergamon) p 172
[31] Staunton J, Strange P, Gyorffy B L, Matsumoto M, Poulter J, Ebert H and Archibald N P 1991 *The Effects of Relativity in Atoms, Molecules and the Solid State* ed S Wilson, I P Grant and B L Gyorffy (New York: Plenum) p 295
[32] Anderson O K, Jepsen O and Sob M 1986 *Electronic Band Structure and its Applications (Lecture Notes in Physics 283)* ed M Yussouff (New York: Springer)
[33] Guo G Y and Temmerman W M 1992 *Mater. Res. Soc. Symp. Proc.* **253** 317
[34] Friedel J 1958 *Nuovo Cimento Suppl.* **7** 287